PERGAMON

International Journal of Heat and Mass Transfer 45 (2002) 831–843

International Journal of HEAT and MASS TRANSFER

www.elsevier.com/locate/ijhmt

Secondary flow and forced convection heat transfer near endwall boundary layer fences in a 90° turning duct

Cengiz Camci *, Dean H. Rizzo

Turbomachinery Heat Transfer Laboratory, Department of Aerospace Engineering, The Pennsylvania State University, 223 Hammond Building, University Park, PA 16802, USA

Received 11 July 2000; received in revised form 11 May 2001

Abstract

The present study deals with the secondary flow and heat transfer aspects of endwall boundary layer fences in 90° turning ducts. Boundary layer fences have recently been re-introduced as additional components to achieve favorable aerothermal effects in turbine/compressor passages and internal cooling systems. The turbine passage or internal coolant channel is simulated by a 90° turning duct ($Re_D = 360{,}000$) to study the aerothermal interaction of the boundary layer fence and the passage flow that is dominated by the passage vortices. Specifically, a single boundary layer fence of varying dimensions is attached to a heated endwall of the duct. The current study adds to the currently small number of investigations on the use of endwall boundary layer fences and their aerothermal interaction with the passage flow system.

1. Introduction

1.1. Purpose

The benefits of increasing the gas turbine efficiency by only a few tenths of a percent are still very attractive. The method of increasing turbine inlet temperature to achieve higher efficiency requires increased coolant effectiveness or a higher maximum allowable temperature of hot section materials. The importance of knowing the heat transfer levels and distribution on turbine passage surfaces is significant. Minimizing coolant flow by putting it where it is needed reduces costly design iterations and decreases durability problems due to hot spots. Another method of increasing the turbine efficiency is reducing the pressure losses by reducing secondary flow related losses. The three-dimensional flow-field present in the turbine has been adequately visualized to capture the complex interaction of many factors such as turbulence, pressure gradient, passage vortices, and horseshoe vortices [1]. However, complete understanding of the role of each of these aerodynamic factors in loss generation is not evidenced in current prediction methods. This investigation deals with controlling/modifying aerodynamic losses due to secondary flows in the passage and heat transfer to the endwall surface via forced convection.

Modern gas turbines contain blade-to-blade passages with low aspect ratio that have strong secondary flows. This study uses a large-scale, curved duct with a square cross-section to simulate the turbine passage without introducing the characteristic horseshoe vortices of a typical cascade arrangement. Extensive flow-field mapping of the duct used in this study and counter-rotating passage vortices were presented in [2]. The inlet boundary layer is fully turbulent and $Re_D = 3.6 \times 10^5$. A single boundary layer fence is attached to one endwall of the duct in an effort to reduce the secondary kinetic energy of the passage vortex flow near the endwall. The dimensions of the fence (length, height, and width) are varied, but all are placed at the mid-passage location between suction and pressure surfaces. The effects of the fence on the flow-field and aerodynamic losses are measured using a five-hole probe in the 90° plane of the duct as described in Fig. 1. Several fence configurations having significant impact on secondary flow near the

* Corresponding author.
E-mail address: c-camci@psu.edu (C. Camci).

0017-9310/02/$ - see front matter
PII: S0017-9310(01)00181-8

Nomenclature

C_{pt}	total pressure coefficient $= (P_{t,in,cl} - P_t)/0.5\rho U_{in,cl}^2$
C_{ske}	secondary kinetic energy coefficient $= (V^2 + W^2)/U_{in,cl}^2$
D	duct width (m)
h	heat transfer coefficient (W/m^2 K), also fence height
k	thermal conductivity of Plexiglas (W/m K)
P	local static pressure (N/m^2)
q	heat flux rate (W/m^2)
Q	total mean velocity
PS	pressure side
R_i, R_o	duct inner and outer radius (m)
Re_D	Reynolds number based on duct width D and inlet bulk velocity $= UD/v$
SS	suction side
T	mean temperature (°C)
Tu	turbulence intensity $= \mathrm{rms}(u')/(U^*100)$
U, V, W	mean velocity components (m/s)
X, Y, Z	streamwise, radial, and spanwise directions
δ_{95}	uncertainty based on 95% coverage
δ_{99}	boundary layer thickness at the rate of $U/U_{in,cl} = 0.99$ (mm)
ρ	density (kg/m^3)
v	kinematic viscosity (m^2/s)

Subscripts

a	ambient (outside duct)
cl	duct centerline
cond	conductive
conv	convective
gen	generated
in	inlet
rad	radiative
t	total or stagnation
∞	free-stream (inside duct)

Superscript

f	passage averaged

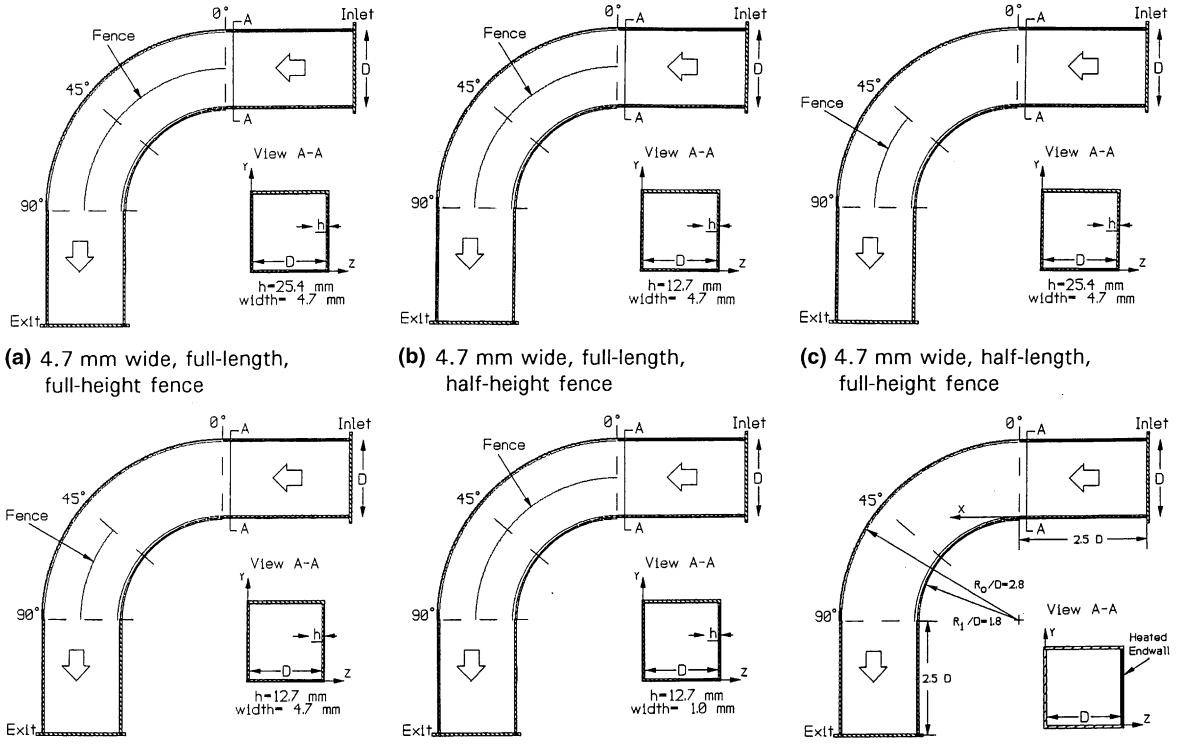

(a) 4.7 mm wide, full-length, full-height fence

(b) 4.7 mm wide, full-length, half-height fence

(c) 4.7 mm wide, half-length, full-height fence

(d) 4.7 mm wide, half-length, half-height fence

(e) 1.0 mm wide, full-length, half-height fence

(f) no fence

Fig. 1. 90° duct with fence configurations X, Y, Z = streamwise, radial and spanwise directions.

heated endwall are then used to investigate the heat transfer to the endwall. Liquid crystal thermography is used to obtain high-resolution maps of the convective heat transfer coefficient for the entire endwall surface. Comparisons of aerodynamic flow-field and endwall heat transfer are made with results from the same duct with no fence installed.

1.2. Related investigations

Several recent studies have focused specifically on aerodynamic effects of endwall boundary layer fences in turbine cascades. Kawai et al. [3] used very thin (0.5 mm) fences of varying height and position on both endwalls of a turbine rotor cascade with $Re_c = 4.5 \times 10^5$. They report up to 22% reduction in secondary losses compared to the no-fence cascade configuration. This reduction in loss is closely related to "capturing" the pressure side leg of the horseshoe vortex above the fence, thus, not allowing it to increase the strength of the passage vortex. More recently, Chung et al. [4] used a triangular-shaped endwall fence in a cascade to prevent the pressure-side leg of the horseshoe vortex from washing film-cooling flow off the blade suction surface. They used flow visualization at $Re_c = 2.93 \times 10^5$ and fence height of 11.3 mm. They report reduced aerodynamic losses and improved cooling performance due to the fence effects on the passage vortex. Chung and Simon [5] further investigated endwall boundary layer fences at increased free-stream turbulence levels ($Tu = 10\%$). They concluded that the passage vortex still dominates, the fence reduces the strength of passage vortex, and the fence may still reduce aerodynamic losses in the passage. The present study differs from these past fence studies primarily by isolating the effects of the fence on the passage vortex without the horseshoe vortex system.

There are numerous studies of endwall heat transfer in a cascade over the past 20 years. Resolution of the heat transfer distribution has improved continuously as experimental techniques have progressed from discrete thermocouple studies to those using the heat-mass transfer analogy or liquid crystals. Increased resolution is important because of the complex nature of the flow. Many investigators have shown a relationship between enhanced endwall heat transfer and secondary flow phenomena. Graziani et al. [6], Gregory-Smith et al. [7], Goldstein and Spores [8] and Boyle and Russell [9] conclude that inlet boundary layer thickness affects endwall heat transfer levels, but not the qualitative form of the distribution. Boyle and Russell [9] and Hippensteele and Russell [10] have investigated the influence of Reynolds number on endwall heat transfer. The present study provides a high-resolution fluid mechanics and heat transfer study of the endwall fence in an effort to understand the passage flow physics that may result in aerothermal performance improvements.

2. Test apparatus and procedure

2.1. Facility

The experimental test section made up of Plexiglas and reference coordinate system is presented in Fig. 1. The endwall surfaces are 12.7 mm thick and pressure/suction surfaces are 4.76 mm thick. The duct has a radius ratio, $R_r = (R_i + R_o)/2D$ of 2.3 and a square cross-section of $D \times D = 203 \times 203$ mm^2. Thermal conductivity of the Plexiglas material isen in the construction of the duct model is $k = 0.1875$ W/m K. A heat transfer composite surface using resistive heating in a thin foil (Inconel 600, 0.0254 mm thick) covered by black paint and several layers of encapsulated chiral nematic liquid crystals (R35C1W) is built on one endwall. The Inconel foil extends from 508 mm upstream of 0–20 mm downstream of 90° as shown in Fig. 1. Four k-type, thin-film thermocouples are attached to the surface of the foil (under the paint and liquid crystals) using double-sided tape that is thermally conductive, but electrically insulated. The non-intrusively mounted thermocouples are used for liquid crystal calibration. Two 500 W incandescent lamps are used for illumination during calibration and experiment. The test section inlet is connected downstream of an open-loop wind tunnel consisting of axial fan, screened diffuser, plenum chamber, high area-ratio circular nozzle, circular to square transition nozzle, and constant cross-section duct. Two different widths of rectangular-shaped boundary layer fences are constructed. "Thick" boundary layer fences are 4.7 mm wide and made of two strips of Plexiglas glued together to maintain a 90° arc. A "thin" fence is 1.0 mm wide and made of stainless steel for rigidity. All fences are thermally insulated on the bottom to minimize conduction from the endwall to the fence. All fence leading and trailing edges are tapered and the top surfaces are beveled. Complete details of the facility and fences are given in [11,12].

2.2. Aerodynamic measurements

All aerodynamic measurements were obtained using a sub-miniature five-hole probe in the non-nulled mode at the 90° plane. The probe head is 1.68 mm and the stem is 3.18 mm in diameter. Total and static pressure and the three velocity components including pitch and yaw angles are simultaneously determined. The probe was calibrated using the method described by Treaster and Yocum [13] for the −30° to +30° range in pitch and yaw at the test case Reynolds number of 360,000. A commercial A/D data acquisition system allowed time averaging of 1000 samples obtained over a 4-s interval.

Six different fence configurations were tested: four thick-fence configurations of varying height and length, one thin-fence configuration, and the baseline no-fence

case. All fences were placed on the heated endwall midway between pressure and suction surfaces using the same attachment points as shown in Fig. 1. Z-axis is imbedded on the suction surface along the height of the duct that coincides with the spanwise direction. Y-axis is in radial direction between the suction surface and pressure surface. The observer (facing the flow) is looking into the duct from an outside location in Figs. 3–7 (90° plane). "Full-length" fences extended from 0° to 90° and "half-length" fences extended from 45° to 90°. "Full-height" fences were approximately equal to the inlet boundary layer thickness (25.4 mm) and "half-height" fences measured 12.7 mm. A 30×30 measurement grid at the 90° plane was used for each case using a computer-controlled traversing mechanism. The digitally controlled stepping motors of the traverse system ensured very accurate placement of the probe. The measurement grid was 5 mm from the duct surfaces to minimize wall interference effects.

2.3. Heat transfer measurements

Heat transfer measurements were made for two different fence configurations: one thick fence (4.7 mm wide, full-length, half-height) and the thin-fence (1.0 mm wide, full-length, half-height). These were compared with the endwall heat transfer for the no-fence case presented in [2]. The heat transfer to the endwall surface was determined for steady-state conditions using liquid crystals and thin-foil resistive heating. A complete description of the technique is given in [14]. The convective heat transfer coefficient on the endwall surface was determined using $h = q_{\text{conv}}/(T_{\text{w}} - T_{\infty}) = (q_{\text{gen}} - q_{\text{cond}} - q_{\text{rad}})/(T_{\text{w}} - T_{\infty})$. A finite element numerical code discussed in [15] was used to determine the non-uniform heat flux generated in the thin foil. The code determines voltage potential distribution in the foil, $V(x, y)$, by solving the electrostatic boundary value problem governed by the Laplace equation. The electric field vector, $\vec{E}$ (V/m), and current density vector, $\vec{J}$ (A/m^2), are determined from the calculated voltage potential distribution. The generated surface heat flux is determined using $q_{\text{gen}} = \delta \cdot (\vec{E} \cdot \vec{J})$, where δ is the foil thickness (m). Conduction from the Inconel foil to the endwall was estimated using a one-dimensional heat loss analysis. A detailed heat loss analysis for the same heat transfer surface exists in [14]. A hue-capturing technique based on liquid crystal thermography, detailed in [16], is used to measure the endwall surface temperature.

2.4. Uncertainty analysis

Uncertainty levels for measured and derived values have been estimated using the procedure of Abernathy et al. [17]. Table 1 summarizes the results based on 20:1 odds. Ref. [11] contains a complete description of sources of error and uncertainty analysis for the experimental measurements presented in this paper.

Table 1
Experimental uncertainty

Data		Uncertainty
$\delta\{U\}$	±0.26 m/s	[1.04% at $U = 25$ m/s]
$\delta\{(V^2 + W^2)^{0.5}\}$	±0.30 m/s	[3.0% at $(V^2 + W^2)^{0.5} = 10$ m/s]
$\delta\{C_{\text{pt}}\}$	±0.015	
$\delta\{h\}$	±4.9 W^2 K/m	[4.9% at $h = 100$ W^2 K/m]

3. Experimental results and discussion

3.1. Overall flow-field and aerodynamic losses

The inlet boundary layer profile and turbulence intensity measured at $X/D = 2.75$ upstream of 0° on the endwall is shown in Fig. 2. $X = 0$ is attached to 0° cross-section as shown in Fig. 1. Measurement of the entire inlet plane revealed relatively uniform boundary layer thickness on all four surfaces. Characteristics of the inlet boundary layer as reported in Wiedner and Camci (1993b) are: $\delta_{0.99} = 25.4$ mm, displacement thickness = 4.6 mm, momentum thickness = 2.6 mm, and shape factor = 1.8. Turbulence intensity ranges from 0.7% in the free-stream to 6.8% at the edge of the measurement grid, $Z/D = 0.975$.

Fig. 3 shows the total pressure fields measured at the exit plane (Y–Z) for all fence cases. This figure shows computer-generated images of the measured five-hole probe-based total pressure interpolated over a 30×30 measurement grid. Different fence configurations

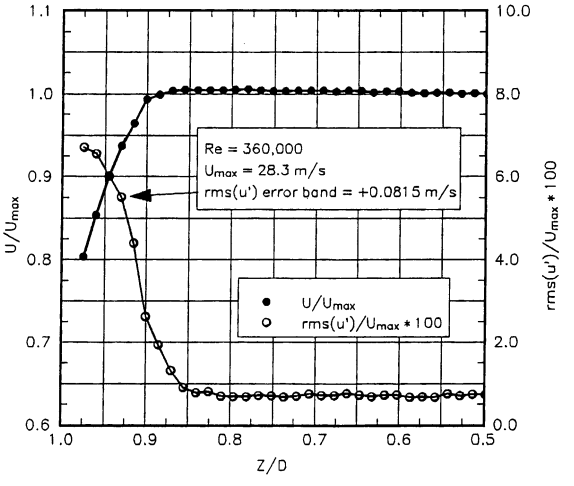

Fig. 2. Boundary layer profile and turbulence intensity at the duct inlet.

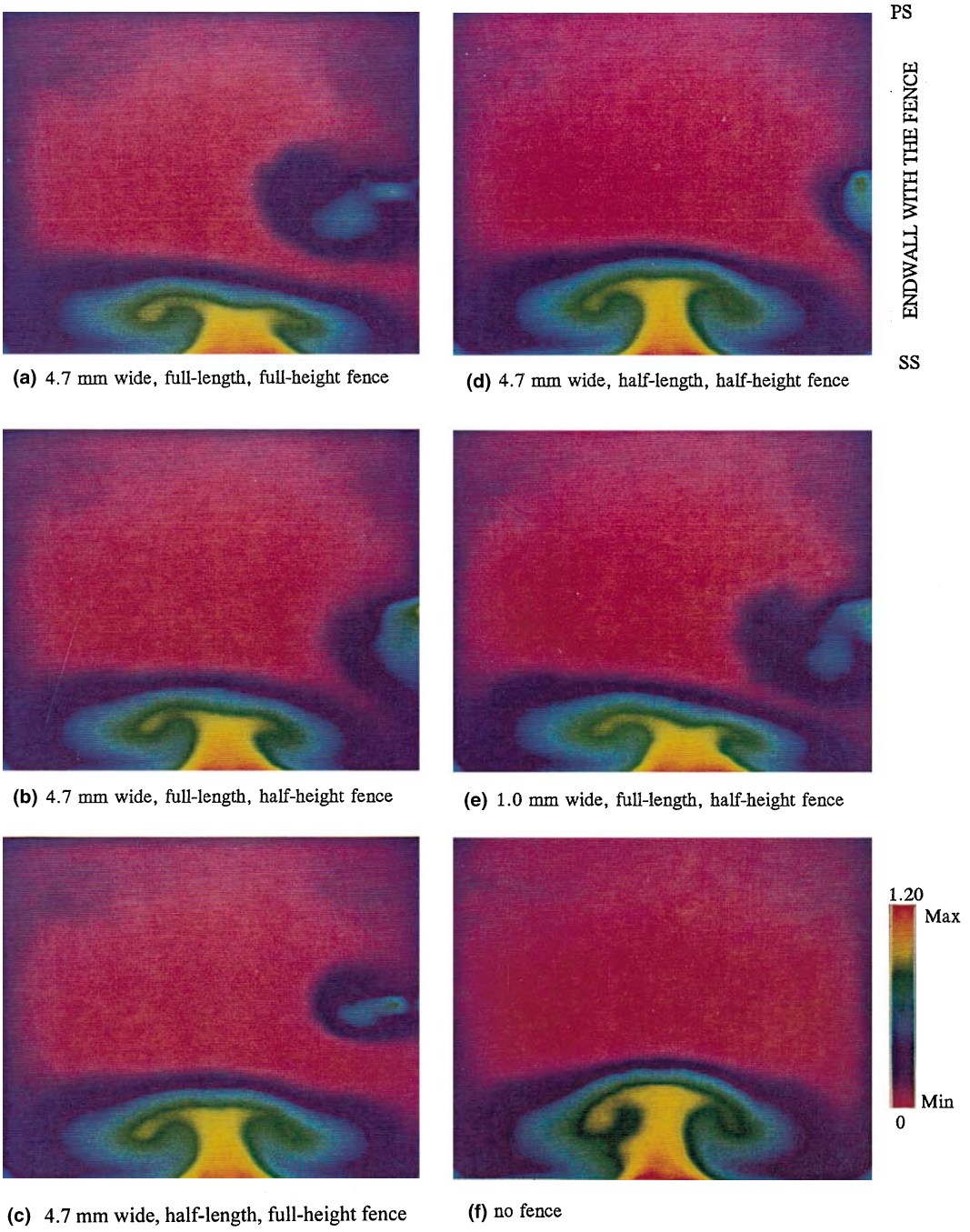

Fig. 3. Total pressure coefficent, $C_{pt} = (P_{t,in,cl} - P_t)/0.5\rho U^2_{in,cl}$ (90° plane).

presented in Fig. 1 are shown in the same order for all figures (e.g., the no-fence case is always shown last). All values are non-dimensionalized with the inlet centerline dynamic pressure. Fig. 3 is shown to portray the trade-off between an additional momentum deficit due to the fence near the endwall and the modification to the flow-field near the suction surface. The action of the passage vortex sweeping low momentum fluid from the concave wall (PS) to the convex wall (SS) is interrupted to varying degree by each fence case. The action of the low momentum fluid in cross-flow region is influenced by fence height and length. The full-length fences influence

total pressure loss over a greater region of the duct than the half-length fences. Viscous losses in the duct are detected as total pressure losses that are concentrated in the passage vortex region near the duct centerline on the suction surface in the no-fence case. The cumulative effect is the high-loss core seen in Fig. 3(f).

The fence reduces the high-loss core by forcing the passage vortex into the free-stream flow where it is convected downstream further before it can combine with the high-loss fluid from the opposite endwall. This is depicted graphically in Fig. 3 by the distortion and translation of the characteristic "mushroom" shape of the high-loss core on the suction surface. All fence cases distort the high-loss core to some degree. The shortest and lowest fence, Fig. 3(d), has the least impact. The longest and highest fence has the greatest impact on the high-loss core. The high-loss core is visibly pushed against the suction surface on the fence side and the center has moved from $Z/D = 0.51$ (for the no-fence case) to $Z/D = 0.58$ in Fig. 3(a). The flow-field modification of the full-height, full-length fence as shown in Fig. 3(a) also shifts the loss core towards the endwall surface corner. To have an overall positive loss reduction effect the fence must not just redistribute the boundary layer fluid, it must reduce losses that are continuously consuming mean kinetic energy of the flow. The fence acts as a mechanical device to resist the transport of low momentum fluid near the endwall by the passage vortex into the high-loss core. Fig. 3 can be used quantitatively to show the trade-off between additional fence losses and reduced passage vortex losses. The total pressure coefficient and secondary kinetic energy for all fence cases are passage averaged at the 90° plane and presented in Table 2. Both full-height fences add to the overall total pressure loss compared to the no-fence case. All three half-height cases (two thick fences and one thin) reduce the total pressure loss in the duct in agreement with the findings of Kawai et al. [3] for a cascade. The half-length, half-height fence of case (d) reduces total pressure loss even greater than the thin, full-length fence of case (e). This is an evidence that there is an optimum fence length as well as a critical fence height for reducing total pressure loss. The passage vortex is still relatively weak at 45°, very similar to measurements performed in [2] for the same duct. Fig. 3(d) shows that a half-length fence is long enough to weaken the passage vortex without adding excessive viscous loss.

Fig. 4 is a graphical explanation of where the change in pressure loss occurs across exit plane between a fence case and the no-fence case. The comparison is made at each measurement point over a 30×30 grid and the "zero" plane represents the total pressure loss for the no-fence case. Thus, areas below the zero plane represent reduced total pressure loss due to a weaker passage vortex (reduced cross flow) on the fence side and areas above the zero plane represent increased pressure loss due to the fence. Fig. 4 offers the best representation of the total pressure loss reduction and enhancement mechanisms in the duct with the endwall fence. The full-length fences reduce the total pressure losses due to the passage vortices significantly (from no-fence level). However, these gains can be diminished by the losses generated in the viscous flow region near the fence. The color map of relative total pressure changes because of the fence which uses green color for zero change where the fence does not alter the no-fence total pressure distribution. There is an increased total pressure loss zone around the fence as revealed by yellow/orange/red colors. The existence of the fence clearly weakens the conventional passage vortex near the suction side where a mushroom pattern (see Fig. 3(f)) for the total pressure exists. The purple colored zone in Fig. 4 indicates a reduced total pressure loss zone in the passage vortex interaction area.

3.2. Secondary flow-field

The fence changes the magnitude and direction of secondary flow along the endwall substantially. Fig. 5 shows the change in secondary flow vector magnitude, $(V^2 + W^2)^{0.5}/U_{\text{in,cl}}$, along the fence endwall in Y–Z plane at the 90° cross-section. Current measurements show that the fence cases with the highest amounts of total

Table 2
Comparison of integral aerodynamic characteristics at 90° plane

	Total pressure coefficient, C_{pt}	%ch	Secondary kinetic energy, $(V^2 + W^2)/U^2_{\text{in,cl}}$	%ch
(a) Full-length, full-height	0.182	+8.9	0.139	+13.9
(b) Full-length, half-height	0.165	−1.2	0.135	+10.7
(c) Half-length, full-height	0.173	+3.6	0.140	+14.8
(d) Half-length, half-height	0.156	−6.5	0.125	+2.5
(e) Full-length, half-height, thin	0.159	−4.8	0.129	+5.7
(f) No fence	0.167		0.122	

%ch = percentage change from no-fence case.

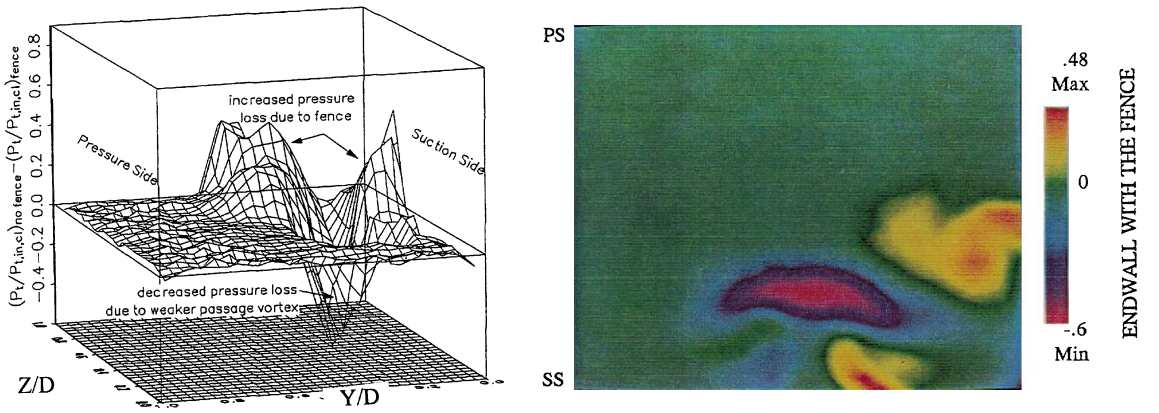

Fig. 4. Total pressure comparison with no-fence case for 1.0 mm wide, full-length, half-height fence $[(P_t/P_{t,in,cl})_{no\ fence} - (P_t/P_{t,in,cl})_{fence}]$ (90° plane, three- and two-dimensional views).

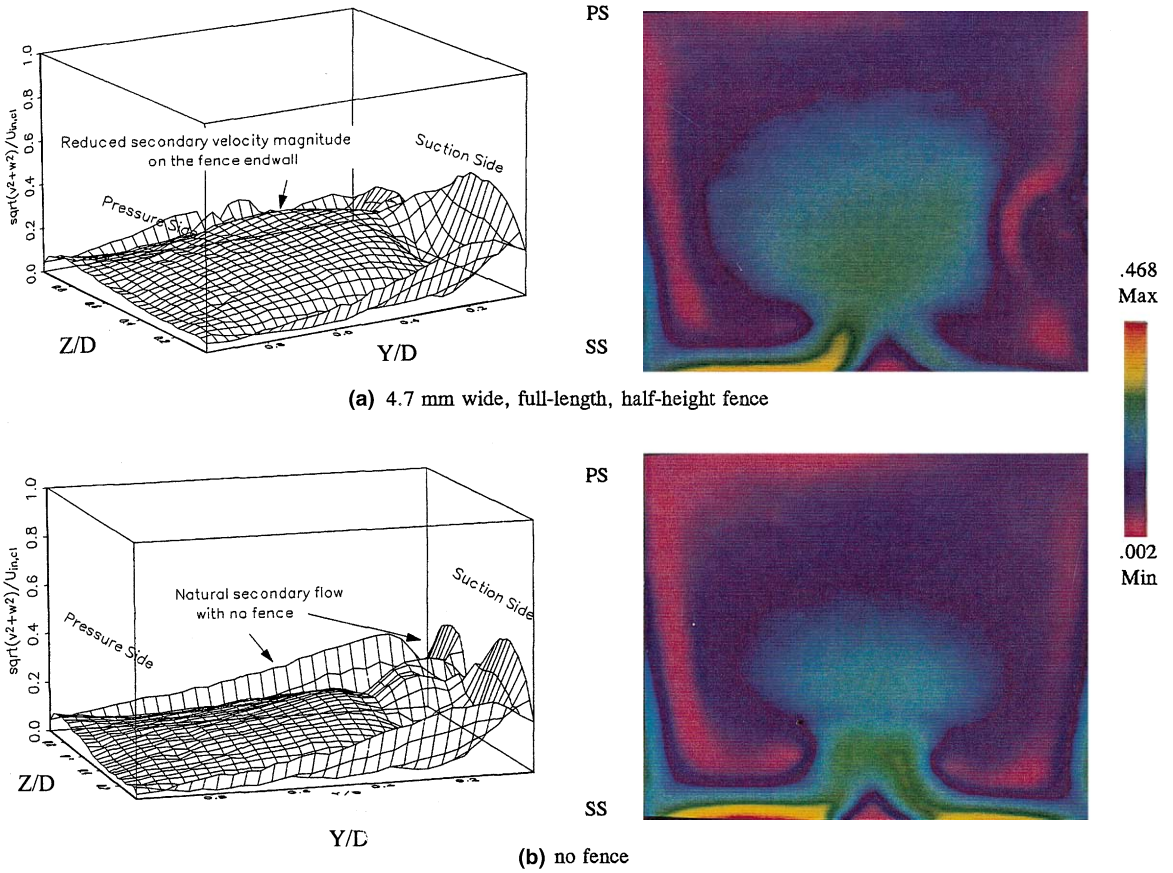

Fig. 5. Mean secondary velocity (90° plane, three- and two-dimensional views).

pressure loss near the endwall region between fence and suction surface, (cases a, b, and e, all full-length cases), are also the fences with the highest secondary flow along the endwall. This is evidence that the full-length fences interrupt the convection of high-loss fluid from the endwall boundary layer by the passage vortex and results in the build-up of that high-loss fluid along the endwall. Fig. 5 presents the mean secondary velocity vector magnitude over the exit plane. Reduced secondary flow magnitude near the endwall (with a full-length/

half-height) fence in Fig. 5(a) is compared with a no-fence measurement. A dark blue zone (with the fence) with reduced secondary velocities and a blue-green zone with full strength secondary velocities (no-fence) is apparent in Fig. 5.

The complex nature of the fence effects on secondary flow is best illustrated by the secondary flow velocity vectors as shown in Fig. 6. All fence cases have interaction of varying strength vortices near the fence endwall. The observed stream-wise vortical structures are

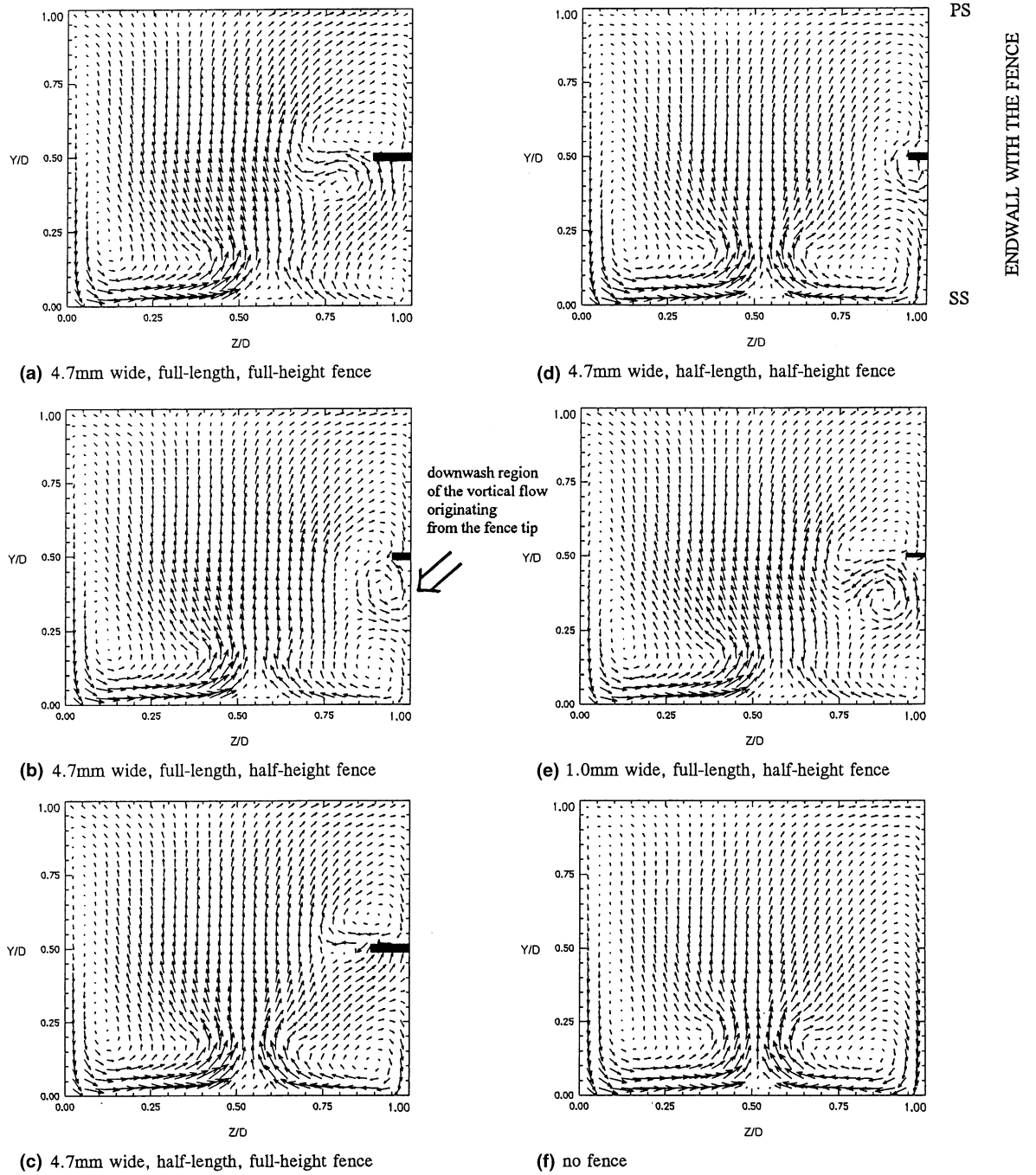

(a) 4.7mm wide, full-length, full-height fence

(d) 4.7mm wide, half-length, half-height fence

(b) 4.7mm wide, full-length, half-height fence

(e) 1.0mm wide, full-length, half-height fence

(c) 4.7mm wide, half-length, full-height fence

(f) no fence

Fig. 6. Mean secondary velocity vectors (90° plane).

associated with endwall heat transfer effects that are discussed in a later section. The full-height cases, Figs. 6(a) and (c), show the fence acting as a blade resulting in two distinct passage vortices developing along the endwall between pressure and suction surface. The thick and thin half-height cases, Fig. 6(b) and (e), develop a pair of counter-rotating vortices between the fence and suction surface as if the fence were a sharp obstacle in the path of secondary flow along the endwall. Another half-height fence, Fig. 6(d), shows the same pair of vortices, but not developed as far as the others since it is a half-length fence. The secondary flow for all the

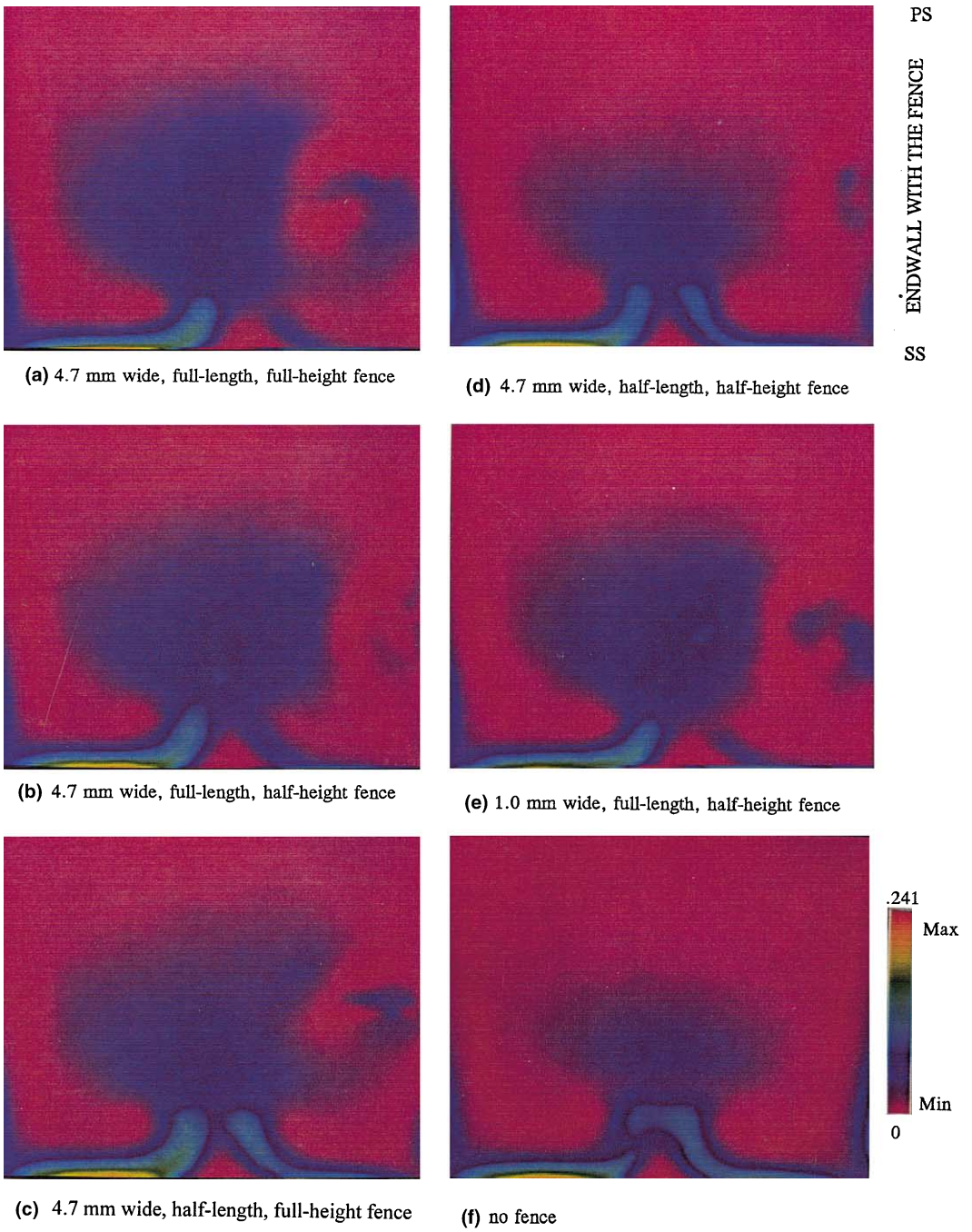

Fig. 7. Secondary kinetic energy (90° plane).

full-length fences is significantly reduced in the endwall/suction surface junction compared to the no-fence and half-length fence cases. All fence cases and the no-fence case display interaction of a passage vortex system on the endwall near the pressure surface at $Z/D = 0.90$. The contour of secondary kinetic energy is clear evidence that the full-length fences, Figs. 7(a), (b), and (e), have reduced the strength of the passage vortex for $Z/D \geqslant 0.5$. Although there is local augmentation of secondary kinetic energy near the fence, the area coverage of this enhancement is not substantial as shown in Fig. 7. However, the dark blue high kinetic energy zone on the endwall surface near the suction side corner is not observed in the cases where a fence alters the passage flow. The secondary kinetic energy reduction is a dominant feature of fence controlled passage vortices near an endwall surface.

3.3. Endwall heat transfer

Endwall heat transfer measurements obtained near the fence are presented in Fig. 8. The flow is from right to left in all three color plots representing the convective heat transfer coefficient (h) distribution. The vertical inlet line is termed "0 degrees" and the horizontal exit line is denoted as "90 degrees" section as shown in Fig. 1. Purple represents low heat transfer levels and red is the highest convective heat transfer coefficient level as quantified in Fig. 8. Details of the heat transfer measurement method based on high-resolution liquid crystal thermography used in this study are explained in [14].

3.4. Thick fence

The endwall heat transfer coefficient distribution for the 4.7 mm wide (thick fence), full-length, half-height fence is shown in Fig. 8(b). At the duct inlet, h increases from pressure to suction side (0°, a vertical line in radially inward direction). The heat transfer influence of the fence is evident at 5° as a dividing line between a region "above" (toward the outer radius) and "below" (toward the inner radius). The fence clearly divides the endwall surface into two regions in terms of the observed heat transfer coefficient distribution. From 5° to 30°, below the fence is a full contour level greater than above the fence. Another noticeable feature from 5° to 45° is the line of constant h running from near the fence

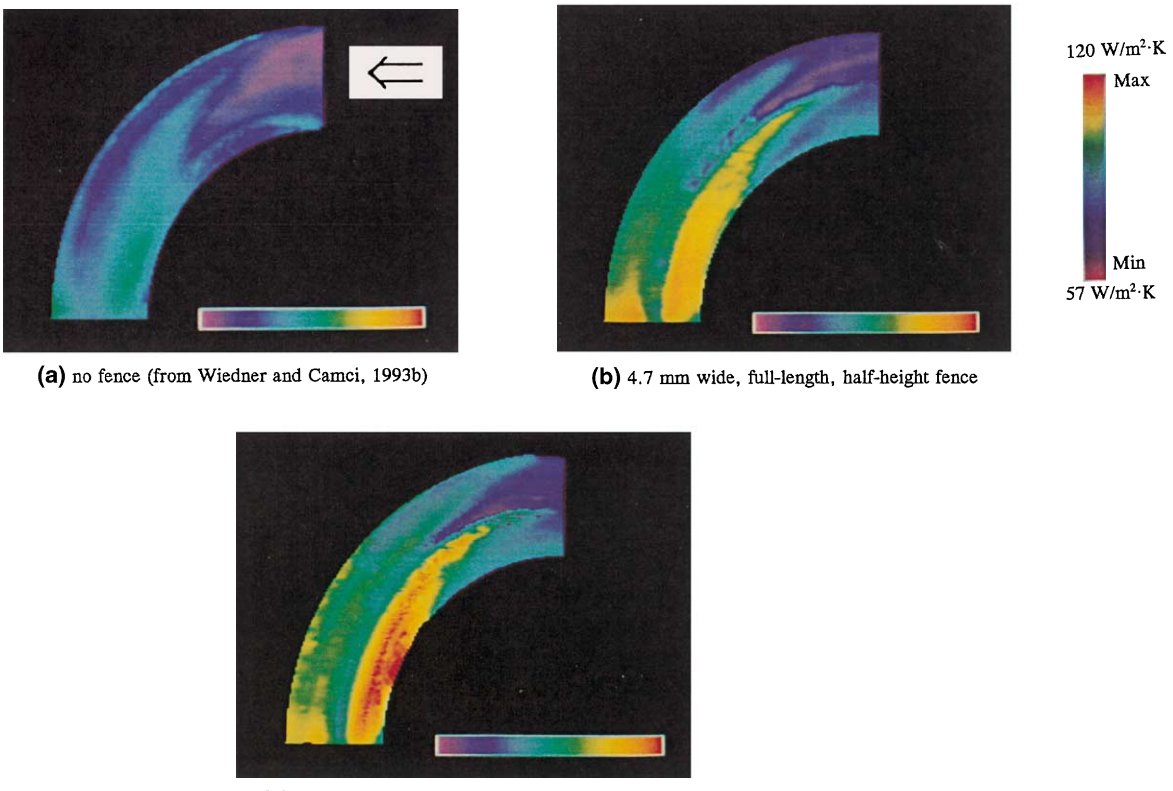

(a) no fence (from Wiedner and Camci, 1993b)

(b) 4.7 mm wide, full-length, half-height fence

(c) 1.0 mm wide, full-length, half-height fence

Fig. 8. Endwall convective heat transfer coefficient distribution (flat endwall surface).

leading edge to the suction side that could correspond to any vortex coming off the fence leading edge. This constant h zone is best described by the color transition from yellow to green. The interaction of a vortical structure induced by the leading edge of the fence with the endwall surface creates a complex three-dimensional heat transfer pattern as shown in Fig. 8(b). At 45°, when the fence is crossed in radially outward direction, a 27% sudden decrease in h is observed as the color changes from yellow/orange to blue across the fence. A large area of fairly high h level (yellow/orange zone) is found between mid-passage and the suction side. This zone corresponds to the down-wash region of the counter-rotating vortices shown in Fig. 6(b). Above the fence, h increases continuously from 45° to 90°. This is associated with a favorable streamwise acceleration in the region above the fence. Installation of a fence usually weakens the secondary kinetic energy of the conventional passage vortex system as presented in Fig. 6(b). Passage vortex strength of the no-fence case (Fig. 6(f)) is much stronger than the vortex strength of the thick-fence case as presented in Fig. 6(b). Fig. 7 also confirms this observation. Installation of a fence, in general, provides a higher level of streamwise kinetic energy to fluid layers near the endwall. The emergence of orange/yellow/green (relatively high h) regions after 45° in Fig. 8(b) in place of the blue dominant h regions of Fig. 8(a) of no-fence case could be explained with the higher streamwise momentum of near endwall fluid interacting with a fence. The emergence of complex vortical patterns near the fence-influenced endwall as presented in Fig. 6 is likely to create highly three-dimensional vortex/endwall interactions. Relatively high heat transfer coefficient levels (orange yellow/green) on the endwall surface are also associated with vortex/endwall interactions. Very close to the exit plane the regions above and below the fence look very similar in distribution and magnitude. The maximum heat transfer at the duct exit plane is between the fence location and pressure surface.

3.5. Comparison of thick fence and no fence

Endwall heat transfer results in the duct with no fence are shown in Fig. 8(a). The thick fence (4.7 mm wide) has changed the magnitude of h significantly in the second half of the duct near the suction side, Fig. 8(b). This is the region where passage vortices normally interact with the endwall surface. The least amount of change is from 0° to 30° where many of the gross patterns are the same and levels are within 10% of each other. Minimum h levels in both cases are found between mid-passage and the duct pressure surface from 0° to 25°. The difference in maximum and minimum h values at 45° for the no-fence case is 15–20% in radial direction. Maximum h levels are present in both cases in the area between mid-passage and the suction surface from 50° to 80°. The thick-fence case maximum h level is approximately 17% greater than the maximum h level for the no-fence case. Heat transfer generally increases from pressure to suction side (for 50–80° section) with local reductions near the fence. In the immediate vicinity of the fence, the retardation of the local streamwise velocity component when compared to no-fence case is responsible from reduced local heat transfer coefficient in limited areas.

3.6. Thin fence

The endwall heat transfer coefficient distribution for the 1.0 mm wide (thin fence), full-length, half-height fence is shown in Fig. 8(c). A corresponding secondary flow map from measurements is also provided in Fig. 6(e) for this case. At 0° h increases from pressure to suction side. At 5° the fence divides the duct endwall into two distinct heat transfer regions above and below the fence. The h levels for the thin-fence case are consistently 10–15% greater than the thick fence levels between 0° and 30° section. The h distribution at 45° is significantly elevated compared to the thick fence. The fence again becomes a distinctive radial demarcation in the h distribution of the thin fence from 45° to 90°. Maximum h level is found between mid-passage and the suction surface, but is 10% greater than the thick-fence case. This coincides with the down-wash of counter-rotating vortices near the endwall as shown in Fig. 6(e). The interaction of the additional streamwise vortex (Fig. 6(e)) due to fence installation with the endwall surface is influential as far as the heat transfer coefficient h is concerned in this area.

3.7. Comparison of thin fence and no fence

Installation of the thin fence certainly weakens the conventional passage vortex system of no-fence case. However, heat transfer coefficient levels observed near the endwall are noticeably elevated in the endwall region between 45° and 90° below the fence line. Fluid mechanics features presented in Fig. 6(e) show that thin fence sets up a strong streamwise vortex on the suction side part of the fence in the region where $0.75 < Z/D < 1.0$ and $0.25 < Y/D < 0.5$. At 0°, the thin-fence h levels are consistently 10–15% greater than the no-fence case. At 50° into the turn, the h values are up to 30% greater than the no-fence case in the region of maximum heat transfer between fence and suction surface. Distributions for the thin-fence and no-fence cases show the same qualitative features radially and streamwise. Minimum h levels in both cases are found between mid-passage and pressure surface from 0° to 25°. Maximum h levels in both cases are found between mid-passage and suction surface from 50° to 80°.

4. Conclusions

The aerodynamic and endwall heat transfer effects are presented for six different endwall boundary layer fences in a 90° turning square duct. The fence dimensions (width, length, and height) are varied, but all are attached to the endwall midway between pressure and suction surfaces. A five-hole probe is used to map the mean pressure, velocity and secondary kinetic energy fields at the 90° plane to identify secondary flow features and aerodynamic losses. Liquid crystal thermography is used to determine the convective heat transfer coefficient distribution for the entire endwall surface.

4.1. Fence effects on secondary flow

1. The full-length fences weaken conventional secondary flow along the endwall the most and also have the largest regions of total pressure loss near the endwall. This is evidence that the fences reduce the amount of low-energy boundary layer fluid that is convected by the passage vortex to the suction surface and that low-energy fluid remains near the endwall.
2. Half-height fences produce a pair of counter-rotating vortices near the fence. Full-height fences act as blades and form two separate passage vortices near the endwall between the fence pressure and suction surfaces and the duct pressure and suction surfaces.
3. All fences tested result in a vortex–endwall interaction between $Y/D = 0.15$ and 0.35 near the corner of the suction side and the fence.
4. All half-height fences reduce the passage averaged total pressure loss measured at 90°, compared to the no-fence duct in agreement with the results of [3] for a cascade. The 4.7 mm wide (thick), 12.7 mm high, long fence achieved the maximum total pressure loss reduction of 6.5% from the no-fence value.
5. Fence dimensions can be optimized due to a trade-off between added viscous and mixing losses due to the fence and the reduction in losses because of a weakened passage vortex.

4.2. Fence effects on forced convection heat transfer near the endwall

1. The boundary layer fence significantly influenced the level of convective heat transfer coefficient on the endwall. In the passage between 0° and 30° the fence divided the endwall into two regions. Greater heat transfer between mid-passage and the suction side was observed in this region. Minimum h levels in both fence cases and the no-fence case were found between mid-passage and the pressure surface from 0° to 25°.
2. Both the thick and thin fences increased the endwall heat transfer throughout the turning duct. Heat transfer enhancement was the greatest for the thin (1.0 mm wide), full-length, half-height (1/2 the inlet boundary layer thickness) fence positioned at mid-passage achieving an enhancement of 20% at 50°. Endwall heat transfer was enhanced up to 30% in the region of maximum heat transfer between fence and suction surface from 50° to 80°.
3. The increasing heat transfer levels for both fence cases and the no-fence duct between mid-passage and the pressure surface from 45° to 90° coincide with a favorable streamwise pressure gradient.
4. The maximum heat transfer levels seen in both fence cases coincides with the interaction of counter-rotating vortices formed near the endwall between fence and suction surface. Maximum h levels in all cases were found between mid-passage and suction surface from 50° to 80°.
5. The fence configurations providing a reduction in passage averaged total pressure loss and simultaneously enhancing endwall heat transfer (compared to the no-fence case) can be effectively used in the design of internal cooling passages. Enhanced heat transfer and simultaneous total pressure loss reduction are two significant "endwall-fence" features that can be used in cooling passage designs using 90° turns.

Acknowledgements

The authors are indebted to the US Military Academy at West Point for the fellowship they have provided to Dean Rizzo during his graduate study at the Pennsylvania State University. Acknowledgements are also due to Dr. K. Kim and Dr. B.G. Wiedner for their continuous support in liquid crystal heat transfer measurements and aerodynamic measurements throughout this study.

References

[1] C.H. Sieverding, Recent progress in the understanding of basic aspects of secondary flows in turbine blade passages, Trans. ASME J. Eng. Gas Turbines Power 107 (1985) 248–257.

[2] B.G. Wiedner, C. Camci, Passage flow structure and its influence on endwall heat transfer in a 90° turning duct: mean flow and high resolution endwall heat transfer experiments, Trans. ASME J. Turbomach. 119 (1997) 39–50.

[3] T. Kawai, S. Shinoki, T. Adachi, Secondary flow control and loss reduction in a turbine cascade using endwall fences, JSME Int. J. (Series II) 32 (1989) 375–387.

[4] J.T. Chung, T.W. Simon, J. Buddhavarapu, Three-dimensional flow near the blade/endwall junction of a gas turbine: application of a boundary layer fence, ASME

Paper 91-GT-45, Presented at the 36th ASME International Gas Turbine and Aeroengine Congress and Exposition, 1991.

[5] J.T. Chung, T.W. Simon, Effectiveness of the gas turbine endwall fences in secondary flow control at elevated free-stream turbulence levels, ASME Paper 93-GT-51, Presented at the 38th ASME International Gas Turbine and Aeroengine Congress and Exposition, 1993.

[6] R.A. Graziani, M.F. Blair, J.R. Taylor, R.E. Mayle, An experimental study of endwall and airfoil surface heat transfer in a large scale turbine blade cascade, Trans. ASME J. Eng. Power 102 (1980) 257–267.

[7] D.G. Gregory-Smith, C.P. Graves, J.A. Walsh, Growth of secondary losses and vorticity in an axial turbine cascade, Trans. ASME J. Turbomach. 110 (1) (1988) 1–8.

[8] R.J. Goldstein, R.A. Spores, Turbulent transport on the endwall in the region between adjacent turbine blades, Trans. ASME J. Heat Transfer 110 (1988) 862–869.

[9] R.J. Boyle, L.M. Russell, Experimental determination of stator endwall heat transfer, Trans. ASME J. Turbomach. 112 (1990) 547–558.

[10] S.A. Hippensteele, L.M. Russell, High-resolution liquid-crystal heat-transfer measurements on the end wall of a turbine passage with variations in Reynolds number, NASA TM 100827, 1988.

[11] D.H. Rizzo, Aerodynamic and heat transfer effects of a endwall boundary layer fence in a 90° turning square duct, M.S. Thesis, The Pennsylvania State University, Department of Aerospace Engineering, 1994.

[12] D.H. Rizzo, C. Camci, The effects of a boundary layer fence on the aerodynamic flow field and endwall heat transfer in a 90° turning square duct, in: 1994 ASME Winter Annual Meeting, Session: Heat Transfer in Gas Turbines, ASME bound Volume HTD-300, Chicago, 1994, pp. 83–99.

[13] A.L. Treaster, A.M. Yocum, The calibration and application of five-hole probes, ISA Trans. 18 (1979) 23–34.

[14] B.G. Wiedner, C. Camci, A technique for the determination of local heat flux on steady-state heat transfer surfaces with arbitrarily specified boundaries, Trans. ASME J. Heat Transfer 118 (4) (1996) 1–8.

[15] C. Camci, An experimental and numerical investigation of near cooling hole heat fluxes on a film cooled turbine blade, Trans. ASME J. Turbomach. 111 (1989) 63–70.

[16] C. Camci, K. Kim, S.A. Hippensteele, A new hue capturing technique for the quantitative interpretation of liquid crystal images used in convective heat transfer studies, Trans. ASME J. Turbomach. 114 (1992) 765–775.

[17] R.B. Abernathy, R.P. Benedict, R.B. Dowdell, ASME measurement uncertainty, Trans. ASME J. Fluids Eng. 107 (1985) 161–164.